Motor Constant Maximization

The complexity involved in magnetic design makes it impossible to derive a motor constant expression for a realistic motor that allows one to relate motor constant to motor design parameters. However, an analytic result can be derived by considering the ideal case where the air gap flux density is as shown in Fig. 4-5 and the corresponding flux and back EMFs are as shown in Fig. 4-9. This motor has full pitch windings and one slot per pole per phase, *i.e.*, $N_s = 3N_m$, such as that shown in Fig. 4-11 with end turn construction as shown in Fig. 4-32. In addition, squarewave currents applied to each phase to match the respective back EMFs produce maximum and constant torque.

In the ideal situation, the torque produced by one phase is given by (4.11). With all three phases producing the same torque simultaneously, the total motor torque produced is three times that given by (4.11), or

$$|T| = 6 N_m B_g L_{st} R_{ro} N i \tag{11.9}$$

For this ideal motor, there are N_m coils per phase with each coil having N turns, and each slot contains two coils. As a result, using the general equation for resistance (4.13), the phase resistance can be written as

$$R_{ph} = \rho \frac{2N(L_{st}+L_{end})N_m}{K_{wb}A_{sl}/(2N)} = \rho \frac{4(L_{st}+L_{end})N^2 N_m}{K_{wb}A_{sl}} \tag{11.10}$$

where ρ is the resistivity of the wire, $2N(L_{st} + L_{end})N_m$ is the total length of wire per phase, and $K_{wb}A_s/(2N)$ is the cross-sectional area allocated to a single turn as a function of the slot cross-sectional area A_{sl} in which K_{wb} is the bare wire slot fill factor as defined in (4.39). In addition, L_{st} is the motor stack length and L_{end} is the end turn length, which can be approximated as

$$L_{end} = \frac{\pi^2 R_{so}}{N_m} \tag{11.11}$$

Using (11.10), the total I^2R losses incurred to produce the torque in (11.9) is

$$P = 3 i^2 R_{ph} \tag{11.12}$$

Finally, substitution of (11.9) and (11.12) into the motor constant expression (4.46) leads to the motor constant expression

$$K_m = \frac{T}{\sqrt{P}} = B_g R_{ro} L_{st} \sqrt{\frac{3N_m K_{wb} A_{sl}}{\rho(L_{st}+L_{end})}} \tag{11.13}$$

where the slot cross-sectional area A_{sl}, as described in Fig. 11-1, can be written as

$$A_{sl}=\frac{\pi}{N_s}\left[\left(R_{so}-w_{sy}\right)^2-\left(R_{ro}+g+d_{sht}\right)^2\right]-w_{tb}\left(R_{so}-w_{sy}-R_{ro}-g-d_{sht}\right) \quad (11.14)$$

Based on (11.13), increasing the air gap flux density is the most straightforward way to maximize the motor constant. While motor constant appears to be directly proportional to B_g, increasing the air gap flux density increases the tooth body width (11.4) and stator yoke width (11.7), which decreases the slot cross-sectional area A_{sl}. As a result, motor constant increases nearly linearly with B_g. This strong relationship exists because increasing the air gap flux density contributes directly to the torque in the numerator of (11.13), but only weakly contributes to increased resistance in the denominator.

The influence of the rotor outside radius R_{ro} on the motor constant depends on whether the stator outside radius R_{so} is fixed or variable. If R_{so} increases as R_{ro} increases, motor constant increases linearly with R_{ro}. If R_{so} is fixed, motor constant no longer increases linearly with R_{ro} because increasing R_{ro} decreases the slot cross-sectional area. This phenomenon occurs since the tooth bottom width w_{tb} and stator yoke width w_{sy} increase with R_{ro} and the radial dimension for windings $R_{so} - R_{ro}$ decreases. As R_{ro} approaches R_{so}, the slot cross-sectional area approaches zero. Therefore, an optimum R_{ro} or radius ratio R_{ro}/R_{so} exists that is worth exploring.

Maximizing motor constant by optimizing the radius ratio R_{ro}/R_{so} can be visualized by considering **Fig. 11-2**. Both motor cross sections in the figure describe four pole, twelve slot motors that have the same outside stator radius. Fig. 11-2*a* is a copper motor where there is greater room for windings and less magnet material. On the other hand, Fig. 11-2*b* is a magnet motor, having a larger outside rotor radius. In the magnet motor case, there is less room for windings but significantly more magnet material.

To find the optimum radius ratio R_{ro}/R_{so} requires substituting (11.4), (11.7), (11.11), (11.14) and the fact that $N_s = 3N_m$ into the motor constant expression (11.13). Furthermore, it is convenient to set the lamination stacking factor K_{st} to 1, let the tooth and stator yoke flux densities be equal, *i.e.*, $B_t = B_{sy} = B_s$, and set g and d_{sht} to zero since they are negligible compared to R_{ro}. Defining the stator length to diameter ratio as the ratio of the stack length L_{st} to the stator outside diameter $2R_{so}$

$$\delta_L=\frac{L_{st}}{2R_{so}} \quad (11.15)$$

the radius ratio as

$$\delta_R=\frac{R_{ro}}{R_{so}} \quad (11.16)$$

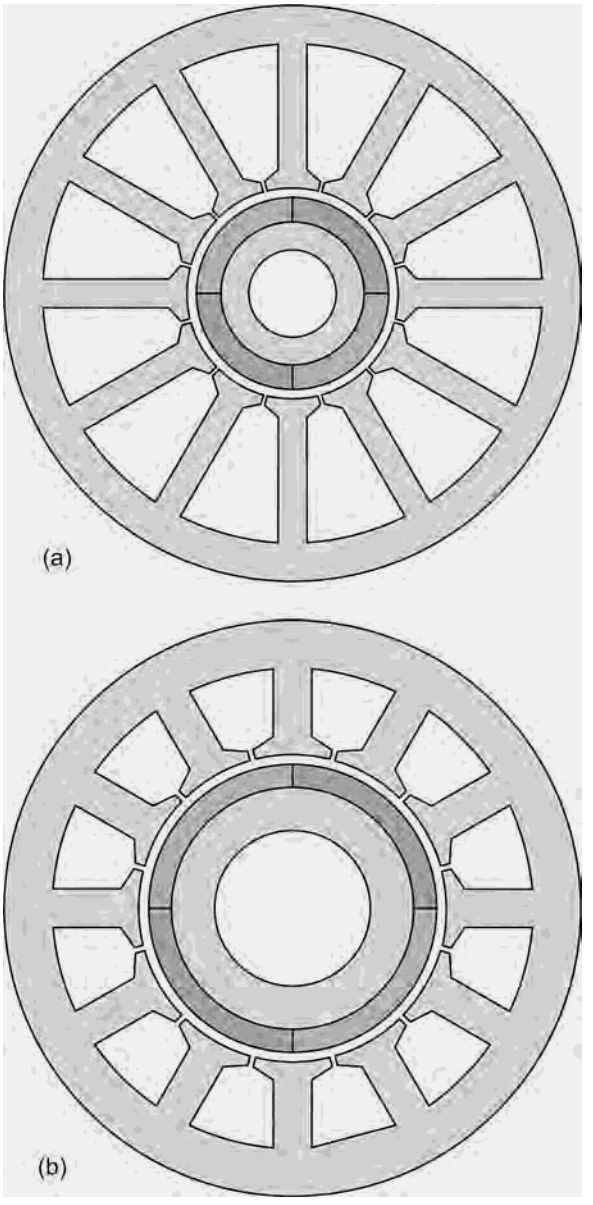

Figure 11-2. Motor cross sections having different outside rotor radii.

the ratio of the stator flux density to the air gap flux density as

$$\delta_B = \frac{B_s}{B_g} \tag{11.17}$$

and simplifying the resulting motor constant equation (11.13) leads to

$$K_m = R_{so}^2 \sqrt{\frac{K_{wb}\pi}{\rho}} \left(\delta_L \sqrt{\frac{2R_{so}}{\delta_L + \pi^2/(2N_m)}} \right) \cdot \left[B_g \delta_R \sqrt{\left(1 - \frac{\pi\delta_R}{N_m \delta_B}\right)^2 - \delta_R^2} - \frac{2\delta_R}{\delta_B}\left(1 - \frac{\pi\delta_R}{N_m\delta_B} - \delta_R\right) \right] \tag{11.18}$$

Written as shown above, the motor constant has several notable features. The central term in parentheses on the first line isolates the influence of the stack length through δ_L, and the final term in square brackets on the second line isolates the effects of air gap flux density B_g, stator flux density through δ_B, and radius ratio δ_R. Since the last term is not a function of R_{so}, δ_L, K_{wb}, or ρ, the optimum radius ratio is not a function of these parameters. Differentiating (11.18) with respect to δ_R, setting the result equal to zero, and solving for the radius ratio gives

$$\delta_R^* = \delta_B \frac{N_m}{4} \frac{3N_m + 3\pi - \sqrt{\pi^2 + 2\pi N_m + N_m^2\left(9 - 16\delta_B + 8\delta_B^2\right)}}{\pi^2 + 2\pi N_m + N_m^2 \delta_B\left(2 - \delta_B\right)} \tag{11.19}$$

For the ideal motor and motor drive being considered here, (11.19) describes the optimum radius ratio $\delta_R = R_{ro}/R_{so}$ that maximizes the motor constant. The optimum radius ratio (11.19) ignores all imperfections, including the negative influence of armature reaction on the air gap flux density B_g. In practice, as the outside radius R_{so} increases, the optimum radius ratio becomes larger than that given by (11.19).

For plotting purposes, it is convenient to consider only the last term contained within the square brackets in (11.18). Calling the last term the normalized motor constant k_m, **Fig. 11-3** illustrates k_m for $B_g = 1$ and $\delta_B = 1.5$ as a function of radius ratio δ_R for various magnet counts N_m. As anticipated, for each N_m, the normalized motor constant has a maximum value. This maximum value identifies the optimum radius ratio as given by (11.19), which is identified by the bold line shown in the figure. For low magnet counts, the optimum radius ratio is near 0.4, whereas, for high magnet counts, the optimum radius ratio is near 0.6. This increase in optimum radius ratio with magnet count is primarily due to the decreasing stator yoke width with increasing N_m as given by (11.7). In all cases, the motor constant is not a strongly influenced by the radius ratio since the curves are relatively flat in the neighborhood of their maximum values. Furthermore, all curves fall more quickly past the maximum since the space for windings diminishes significantly as δ_R approaches one.

Substituting (11.19) into (11.18) and letting $B_g = 1$ and $\delta_B = 1.5$, **Fig. 11-4** shows the influence of magnet count N_m on maximum normalized motor constant. This curve has a saturating characteristic. For low magnet counts, the motor constant

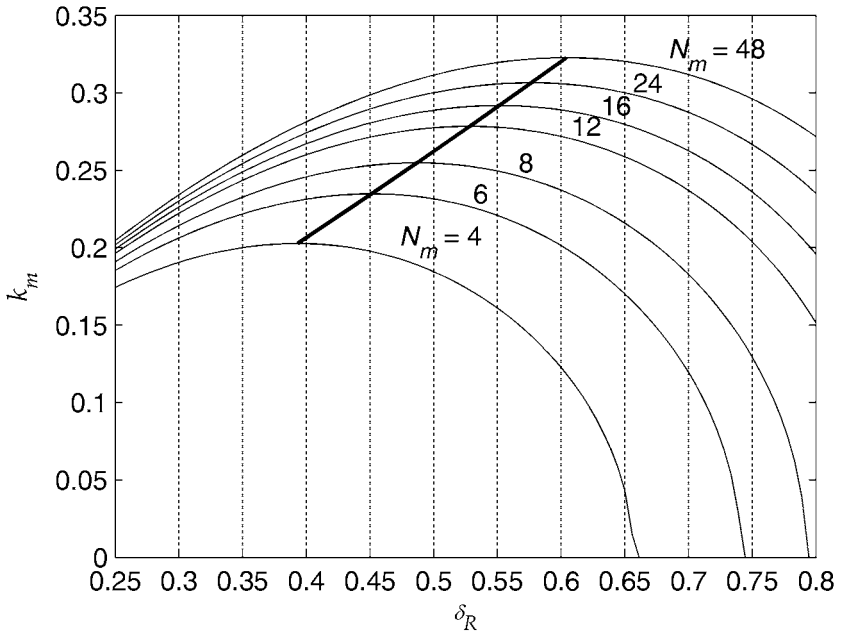

Figure 11-3. Influence of radius ratio and magnet pole count on motor constant.

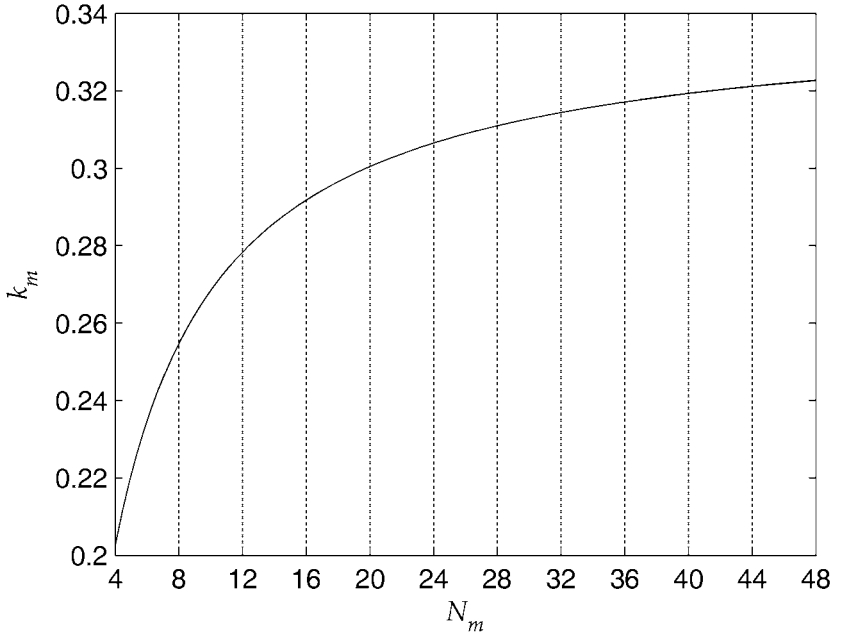

Figure 11-4. Influence of magnet count on maximum motor constant.

increases quickly, whereas, the motor constant does not change much at high magnet counts. Study of both (11.18) and (11.19) shows that as N_m becomes very large, motor constant becomes less and less a function of N_m and approaches an asymptotic value. This fact is confirmed by the decreasing slope of the curve as magnet count increases.

In summary, increasing the air gap flux density is the most significant way to increase motor constant. When the outside stator radius is fixed, the outside rotor radius plays an important but less significant role in maximizing motor constant. When magnet pole count is less than about twenty, increasing the number of magnet poles plays a more significant role than the outside rotor radius. For all cases, increasing the air gap flux density has the greatest significance.

11.2 Torque Saturation

As discussed in the armature reaction section in Chapter 4, the presence of saturating ferromagnetic material in a motor limits its ability to produce torque. In particular, as phase currents increase, the added magnetic flux these currents create competes with the permanent magnet flux in the ferromagnetic parts of the motor, most notably, in the stator teeth. In doing so, the permeability of the ferromagnetic parts of the motor decreases, which increases their reluctance to the flow of torque-producing permanent magnet flux. This increased reluctance decreases the amount of permanent magnet flux that is linked to the phase windings, thereby decreasing the developed torque from that expected based on the assumption of linearity as described by (4.8), (4.11), (9.1), (9.4), (9.9), and (9.32) for example.

Given the myriad of variations involved in motor design, the complex interactions of all instantaneous phase currents, and the magnetic flux these currents create interacting with the rotating permanent magnet flux, torque saturation with increasing phase current is best found using finite element analysis. Predicting torque saturation analytically with a reasonable degree of accuracy is difficult at best. Because finite element analysis can more accurately predict torque saturation, an analytic solution that identifies key parameters and facilitates comparative analysis would provide valuable engineering insight. This section presents an analytic model that attempts to provide insight into torque saturation.

Consider the motor cross section shown in **Fig. 11-5**. Following the single tooth equivalent winding concept first shown in Fig. 7-4, the two single tooth windings shown are part of some more general winding layout. Restricting analysis to the flux that flows through the two slot pitch wide region between the radial lines, leads to the magnetic circuit shown in **Fig. 11-6**. This magnetic circuit is simply a more detailed circuit that that originally considered in Fig. 4-2. In Fig. 11-6, R_t is the stator tooth reluctance, R_{sy} is the stator yoke reluctance, R_g is the air gap reluctance, R_l is a magnet-to-magnet leakage reluctance, and R_r is the rotor yoke reluctance.

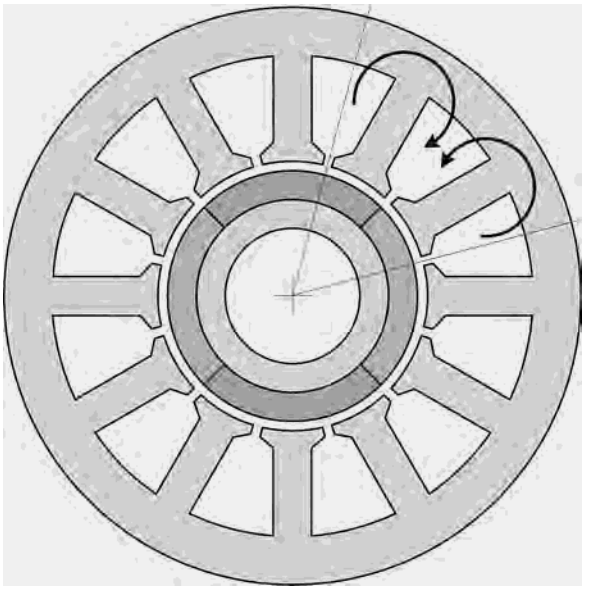

Figure 11-5. A motor cross section showing single tooth coils.

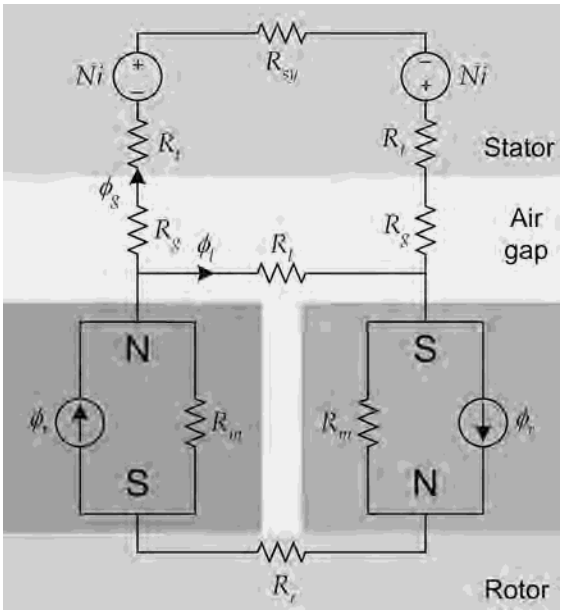

Figure 11-6. Magnetic circuit associated with the motor cross section in Fig. 11-5.

Because stator tooth saturation plays such a major role, it is convenient to ignore the lesser significance of the rotor and stator yokes, and to ignore the leakage flux that does not cross into the stator. Therefore, setting the stator and rotor yoke reluctances to zero, the leakage reluctance to infinity, and simplifying the magnetic circuit leads to the circuit shown in **Fig. 11-7**.

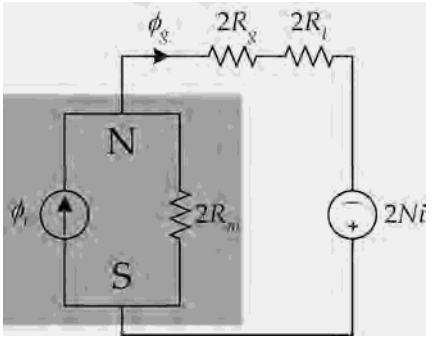

Figure 11-7. Simplification of the magnetic circuit in Fig. 11-6.

The air gap flux ϕ_g in Fig. 11-7 is given by the sum of two components, one due to the permanent magnet ϕ_{pm} and one due to the coil currents ϕ_{Ni}, *i.e.*,

$$\phi_g = \phi_{pm} + \phi_{Ni} \tag{11.20}$$

where

$$\phi_{pm} = \frac{2R_m \phi_r}{2R_m + 2R_g + 2R_t} \tag{11.21}$$

and

$$\phi_{Ni} = \frac{2Ni}{2R_m + 2R_g + 2R_t} \tag{11.22}$$

The corresponding reluctances are given by

$$R_m = \frac{l_m}{\mu_R \mu_o A_{sp}} \tag{11.23}$$

$$R_g = \frac{g}{\mu_o A_{sp}} \tag{11.24}$$

and

$$R_t = \frac{l_t}{\mu_r \mu_o A_t} \tag{11.25}$$

Equations (11.23) and (11.24) follow directly from (4.2), with the exception that cross sectional area here is one slot pitch wide at the inside stator radius R_{si}, *i.e.*,

$$A_{sp} = \tau_s L_{st} \tag{11.26}$$

where $\tau_s = (2\pi/N_s)R_{si}$, and L_{st} is the stack length. The stator tooth has length l_t, cross sectional area

$$A_t = w_{tb} L_{st} \tag{11.27}$$

where w_{tb} is the tooth body width (the presence of shoes is ignored), and the tooth relative permeability is

$$\mu_r = \frac{1}{\mu_o} \frac{B_t}{H_t} \tag{11.28}$$

where B_t and H_t are the flux density and field intensity respectively in the teeth and are obtained from the tooth material *B-H* curve. In this situation, B_t and H_t are influenced by both the permanent magnet flux and the coil current.

Substituting (11.23) through (11.27) into (11.21) and (11.22) leads to

$$\phi_{pm} = \frac{\phi_r}{1 + \mu_R \frac{g}{l_m} + \frac{\mu_R}{\mu_r} \frac{l_t}{l_m} \frac{\tau_s}{w_{tb}}} \tag{11.29}$$

and

$$\phi_{Ni} = \frac{\frac{\mu_R \mu_o \tau_{sp} L_{st}}{l_m} Ni}{1 + \mu_R \frac{g}{l_m} + \frac{\mu_R}{\mu_r} \frac{l_t}{l_m} \frac{\tau_s}{w_{tb}}} \tag{11.30}$$

The net tooth flux density B_t due to both the permanent magnet and the winding current is given by

$$B_t = \frac{\phi_g}{A_t} = \frac{\frac{\tau_s}{w_{tb}} \left(B_r + \mu_R \mu_o \frac{Ni}{l_m} \right)}{1 + \mu_R \frac{g}{l_m} + \frac{\mu_R}{\mu_r} \frac{l_t}{l_m} \frac{\tau_s}{w_{tb}}} \tag{11.31}$$

where $\phi_r = B_r A_{sp}$ has been used to relate the permanent magnet flux source ϕ_r to the remanence B_r.

For a given current *i*, (11.28) and (11.31) can be solved iteratively to find the tooth relative permeability. Substituting (11.28) into (11.31) and describing the stator tooth material *B-H* curve as the function $H_t = \mathrm{hb}(B_t)$ allows (11.31) to be rewritten as

$$f(B_t)=0=B_t-\frac{\frac{\tau_s}{w_{tb}}\left(B_r+\mu_R\mu_o\frac{Ni}{l_m}\right)}{1+\mu_R\frac{g}{l_m}+\mu_R\mu_o\frac{\mathrm{hb}(B_t)}{B_t}\frac{l_t}{l_m}\frac{\tau_s}{w_{tb}}} \tag{11.32}$$

Using a numerical search routine, repeated estimates for B_t leads to the value where f(B_t) is zero. Th B_t value where f(B_t) is zero and the corresponding H_t = hb(B_t) value from the material *B-H* curve substituted into (11.28) gives the relative permeability of the tooth for the chosen current, $\mu_r(i)$. Solving (11.32) over an appropriate range of currents produces a tooth relative permeability function $\mu_r(i)$ as a function of the winding current that in turn influences the torque producing air gap flux density.

The torque producing air gap flux density B_g is that due to the permanent magnet alone. That is, B_g can be found from (11.29) as

$$B_g=\frac{\phi_{pm}}{A_{sp}}=\frac{B_r}{1+\mu_R\frac{g}{l_m}+\frac{\mu_R}{\mu_r(i)}\frac{l_t}{l_m}\frac{\tau_s}{w_{tb}}} \tag{11.33}$$

When the winding current is zero, this equation can be written as

$$B_{go}=\frac{\phi_{pm}}{A_{sp}}=\frac{B_r}{1+\mu_R\frac{g}{l_m}+\frac{\mu_R}{\mu_r(0)}\frac{l_t}{l_m}\frac{\tau_s}{w_{tb}}} \tag{11.34}$$

Together (11.33) and (11.34) provide a way to describe the drop in torque production due to stator tooth material saturation.

Under ideal, nonsaturating material conditions motor torque is directly proportional to B_g, *i.e.*, B_{go} fulfills the role of *B* in the *BLi* law (3.41) and *B* in the ideal torque equation (4.11). Therefore, as the stator teeth saturate and $\mu_r(i)$ decreases from $\mu_r(0)$, the saturated motor torque T_{sat} can be written as

$$T_{sat}=T\frac{B_g}{B_{go}}=T\left(\frac{1+\mu_R\frac{g}{l_m}+\frac{\mu_R}{\mu_r(0)}\frac{l_t}{l_m}\frac{\tau_s}{w_{tb}}}{1+\mu_R\frac{g}{l_m}+\frac{\mu_R}{\mu_r(i)}\frac{l_t}{l_m}\frac{\tau_s}{w_{tb}}}\right) \tag{11.35}$$

where T is the motor torque under ideal, nonsaturating conditions, such as those given in (9.1), (9.4), (9.9), and (9.32). The term in parentheses describes how motor torque decreases as a function of the stator tooth saturation produced by the wind-

ing current i. This term in parentheses can be defined as the torque saturation factor K_{sat} as

$$K_{sat} = \frac{1 + \mu_R \frac{g}{l_m} + \frac{\mu_R}{\mu_r(0)} \frac{l_t}{l_m} \frac{\tau_s}{w_{tb}}}{1 + \mu_R \frac{g}{l_m} + \frac{\mu_R}{\mu_r(i)} \frac{l_t}{l_m} \frac{\tau_s}{w_{tb}}} \tag{11.36}$$

To illustrate torque saturation, **Fig. 11-8** shows a plot of the torque saturation factor for three different magnet and tooth lengths. The ferromagnetic material and other parameters were chosen based on typical usage in motor design. The uppermost curve was computed using a long magnet, $l_m = 10$, and a short relative stator tooth length $l_t/l_m = 25/10 = 2.5$. The other two curves have double the relative tooth length $l_t/l_m = 50/10 = 25/5 = 5$, but have magnet lengths that differ by a factor of two. As expected, short relative stator tooth lengths and longer magnets suffer from less significant torque saturation.

Though not explicitly shown in (11.36), torque saturation is highly influenced by Ni in (11.32). Simply put, the larger Ni is, the more torque saturation occurs. For a given motor Ni is directly proportional to the slot cross-sectional area A_{sl} through (4.45), *i.e.*, $Ni = K_{wb} A_{sl} J$, where A_{sl} is given by (11.14), which shows that A_{sl} grows proportional to the radii squared difference $R_{so}^2 - R_{ro}^2$. Therefore, both A_{sl} and Ni grow in proportion to this radii squared difference. This means that as the motor

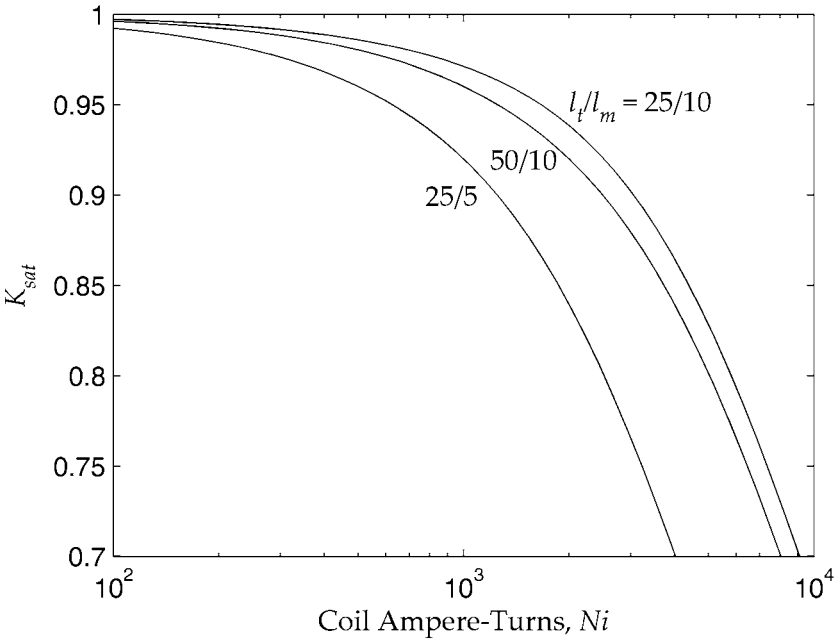

Figure 11-8. Torque saturation factor illustration.

formly over the entire cross section. This outward crowding leaves the inner region of the conductor carrying little or no current. As a result, the effective wire resistance increases. The increase in resistance is determined by the amplitude of the net AC magnetic field experienced by the wire. Just as lamination eddy current losses are reduced by making them thinner, reducing winding wire diameter minimizes the increase in winding resistance. An effective way to reduce effective wire diameter is to use multiple strands of insulated, small diameter wire in parallel in place of an equivalent single strand having larger diameter.

11.8 Motor Drive Limitations

As described in Chapter 9, motor torque is directly proportional to motor current. Simultaneously, ohmic or I^2R losses are directly proportional to the square of motor current. As a result, motor torque production is primarily limited by the ability of the motor drive electronics to drive current into the motor, with the ultimate torque limit set by the thermal capacity to dissipate the heat created by the I^2R losses. Secondarily, core losses, windage, permanent magnet demagnetization, and other characteristics limit performance as well. While these motor physical limits are ultimately important, the limits imposed by the motor drive electronics often impact or limit motor drive system performance first. As a result, they are considered in this section.

Y-Connected Motor Analysis

Since the vast majority of brushless permanent magnet motors are Y-connected the discussion below focuses on the topology as shown in **Fig. 11-14**. This figure is similar to Fig. 9-9, but includes several changes to facilitate and simplify circuit analysis. In Fig. 11-14, the power supply has been split into two sources in series, each having one half the full value V_{cc} shown in Fig. 9-9. The source was split in two so that the circuit reference voltage or ground could be placed in between the two sources. Since the choice of reference voltage is arbitrary, this choice does not influence circuit operation, rather, it simplifies circuit analysis.

In addition to splitting the sources and placing the circuit reference between them, Fig. 11-14 identifies the phase node voltages v_a, v_b, and v_c, which are the respective motor terminal voltages with respect to the circuit reference. The voltage at the center of the Y with respect to the circuit reference is identified as v_n.

Applying Kirchoff's current law at the center of the Y using conventional AC phasor analysis gives

$$\frac{V_a - V_n - E_a}{Z_{ph}} + \frac{V_b - V_n - E_b}{Z_{ph}} + \frac{V_c - V_n - E_c}{Z_{ph}} = 0 \tag{11.77}$$

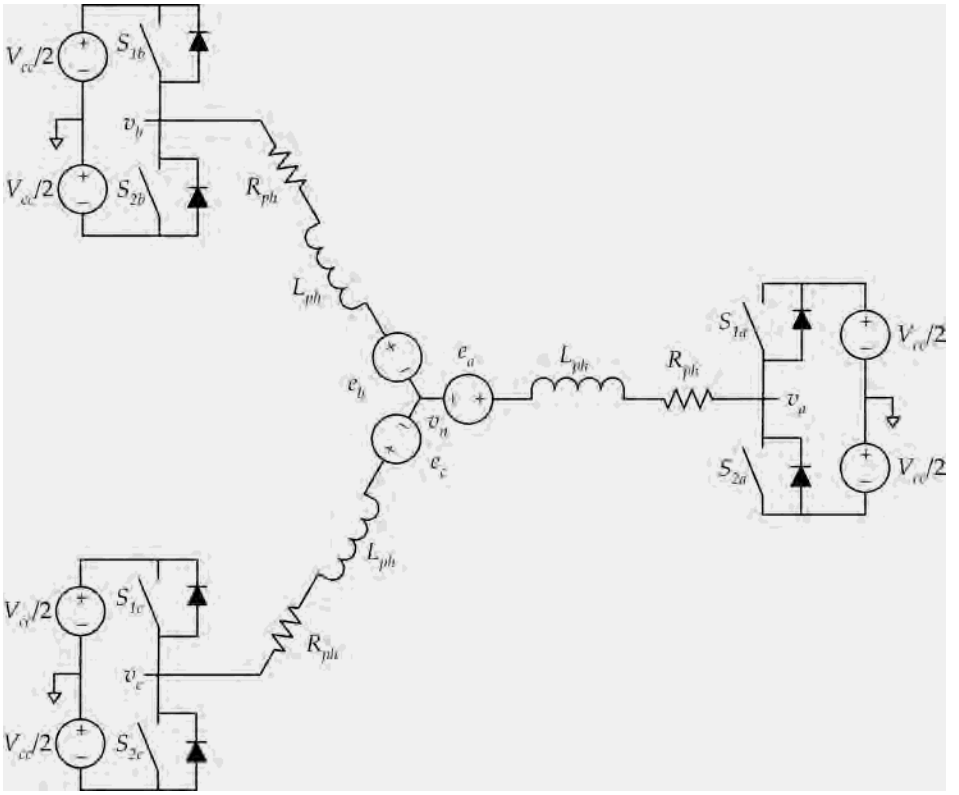

Figure 11-14. Alternative *Y*-connection drive topology.

where Z_{ph} is the combined impedance of R_{ph} in series with L_{ph}. Multiplying through by Z_{ph} eliminates it from this equation and simplifies the equation to an instantaneous relationship that leads to the center node voltage

$$v_n = \frac{1}{3}\left[\left(v_a + v_b + v_c\right) - \left(e_a + e_b + e_c\right)\right] \tag{11.78}$$

Thus, the center node voltage is simply the average of the applied phase voltages less the average of the back EMF voltages. While this analysis ignores the mutual inductance among the phases, the influence of mutual inductance does not change (11.78) since mutual inductance can be combined into the phase inductance as demonstrated in the transition from (10.41) to (10.42) in the preceding chapter.

AC Synchronous Motor Assumption

To facilitate further analysis, it is convenient to restrict the motor terminal voltages and back EMFs to be sinusoidal functions at the fundamental electrical frequency ω_e. This assumption matches the AC synchronous motor drive discussed in Chapter 9. While the motor terminal voltages will PWM between the limits of $-V_{cc}/2$ and $+V_{cc}/2$, the PWM action will act to create near sinusoidal terminal

voltages and resulting phase currents at the fundamental electrical frequency. The exact voltage waveform produced at the motor terminals will have significant harmonics at the PWM frequency and its harmonics. However, because these frequencies are assumed to be much greater than the fundamental electrical frequency, they are ignored in this analysis. To proceed mathematically, it is necessary to ignore the inherent PWM ripple. It is also important to note that this analysis applies equally well to both conventional and vector control schemes.

Under the same symmetry and balance assumptions made in Chapter 9 for the AC synchronous motor drive, the instantaneous sum of the back EMFs as well as the instantaneous sum of the motor terminal voltages are zero, which from (11.78) means that the center node voltage is identically zero, *i.e.*, $v_n = 0$. Under these conditions, the analysis of one phase provides the solution for all phases with a corresponding shift in phase angle to match the phase angle of the associated back EMFs and applied voltages.

Applying Kirchoff's voltage law to the phase A winding in Fig. 11-14 gives

$$v_a = R_{ph} i_a + L_{ph} \frac{di_a}{dt} + e_a \tag{11.79}$$

By letting $\omega_e = \theta t$, where θ is in electrical measure, this differential equation can be recast as a function of electrical position rather than time as

$$v_a(\theta) = R_{ph} i_a(\theta) + \omega_e L_{ph} \frac{di_a(\theta)}{d\theta} + e_a(\theta) \tag{11.80}$$

For a given applied voltage $v_a(\theta)$, (11.80) can be solved for the resulting phase current $i_a(\theta)$. Alternatively, given the phase current, (11.80) can be solved for the applied voltage $v_a(\theta)$ that produces it.

In addition to solving for the current or applied voltage, (11.80) describes the rate at which current can change as a function of position. Solving (11.80) for $di_a(\theta)/d\theta$ gives

$$\frac{di_a(\theta)}{d\theta} = \frac{v_a(\theta) - \left[e_a(\theta) + R_{ph} i_a(\theta) \right]}{\omega_e L_{ph}} \tag{11.81}$$

This equation shows that $v_a(\theta)$ must be greater in amplitude than the sum of the back EMF $e_a(\theta)$ and resistive voltage drop $R_{ph} i_a(\theta)$ to make the current $i_a(\theta)$ increase in value, *i.e.*, make $di_a(\theta)/d\theta > 0$. Since the amplitude of the back EMF increases linearly with speed, the achievable $di_a(\theta)/d\theta$ decreases with increasing speed, which in turn limits the peak current achievable. Other than increasing the amplitude of the applied voltage, an alternative way to maximize $di_a(\theta)/d\theta$ is to advance the phase of the applied voltage relative to the back EMF. In doing so, the applied voltage rises earlier in position θ than the back EMF, thereby creating a

positive voltage difference. This allows current to flow into the winding before it is efficiently used for torque production.

To facilitate further analysis, it is convenient to assume specific forms for the applied voltage, back EMF, and phase current. The applied voltage can be written in the form

$$v_a(\theta) = \frac{V_{cc}}{2} d(\theta) \tag{11.82}$$

where $d(\theta)$ is the PWM duty cycle or modulation function

$$d(\theta) = D\cos(\theta - \delta_d) \tag{11.83}$$

in which the duty cycle amplitude or modulation index D is such that $0 \le D \le 1$ and δ_d is the phase angle of the applied voltage. This description models the behavior of PWM schemes that ideally produce sinusoidal currents.

PWM schemes that support D > 1 are said to provide overmodulation. A simple way to visualize overmodulation is to consider a controller request for D greater than 1, but then recognize that $|d(\theta)|$ is limited to one by the power supply limits (11.82) as shown in **Fig. 11-15**. Even though $|d(\theta)| \le 1$, the amplitude of the fundamental harmonic component in the clamped waveform exceeds one. Therefore, the effective duty cycle amplitude D for the fundamental harmonic is greater than one.

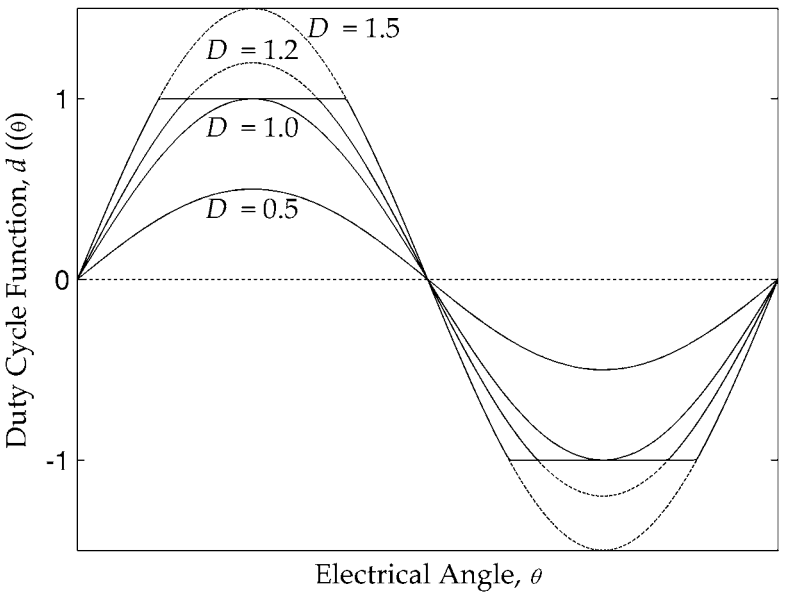

Figure 11-15. Supply voltage clamping due to overmodulation.

For the clamping scenario shown in Fig. 11-15, the relationship between the requested and effective D is shown in **Fig. 11-16**. As shown in the figure, when $D \leq 1$, the achieved duty cycle matches the requested duty cycle. However, in the overmodulation region the achieved duty cycle saturates with increasing requested values.

While overmodulation allows one to achieve a greater effective modulation index, doing so introduces current harmonics due to the harmonics introduced into the applied voltage (11.82) by the clamped duty cycle function shown in Fig. 11-15. These current harmonics increase the winding I^2R losses, but do not increase the torque produced when the back EMF is sinusoidal. Therefore, motor efficiency decreases in the overmodulation region, which is already a high loss region. In addition, overmodulation makes the relationship between requested and achieved duty cycle amplitude nonlinear as shown in Fig. 11-16, which can affect motor controller performance.

Using (9.8), the phase A back EMF can be written as

$$e_a(\theta) = K_p \omega_m \cos(\theta) \tag{11.84}$$

where K_p is the amplitude of the back EMF shape, and ω_m is the speed in radM/s. To give K_p meaning relative to the circuit driving the motor, it is beneficial to normalize the back EMF to $V_{cc}/2$ as

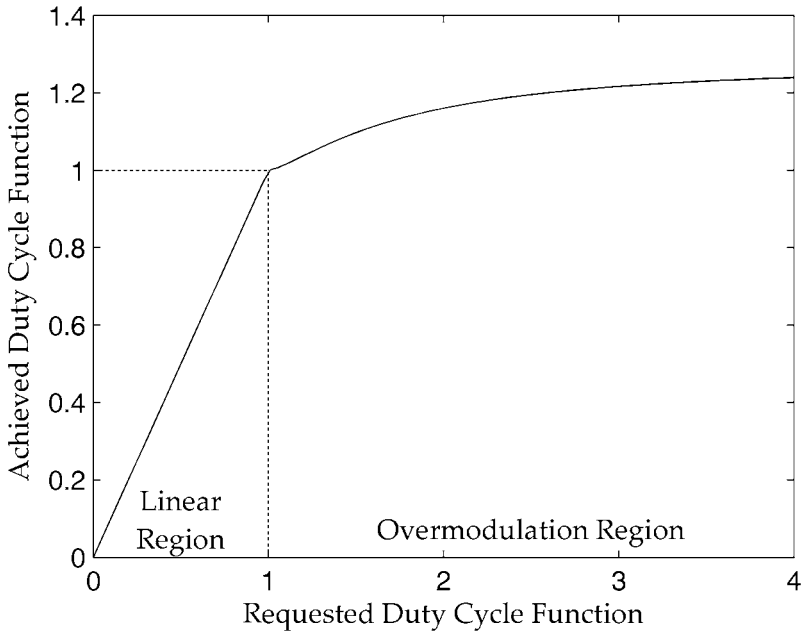

Figure 11-16. Requested versus achieved duty cycle in overmodulation region.

$$e_a(\theta)=\left(\frac{V_{cc}}{2}\frac{\omega_e}{\omega_{cc}}\right)\cos(\theta) \tag{11.85}$$

where ω_e is the motor speed in radE/s, ω_{cc} is the motor speed at which the back EMF voltage amplitude is equal to $V_{cc}/2$, that is, when $\omega_e = \omega_{cc}$, $\max(e_a(\theta)) = (V_{cc}/2)$. Setting (11.84) equal to (11.85) and solving for K_p gives

$$K_p=\frac{V_{cc}N_m}{4\omega_{cc}} \tag{11.86}$$

It is important to note that (11.84) and (11.85) are not the line-to-line back EMF that is measurable at the motor terminals, but rather the phase back EMF measurable from line to neutral. Because the back EMF is sinusoidal, the amplitude of phase back EMF is equal to the line-to-line back EMF divided by $\sqrt{3}$ as per standard three phase sinusoidal analysis.

Finally, the phase current can be written as

$$\begin{aligned} i_a(\theta) &= I_p\cos(\theta-\delta_i) \\ &= \left[\frac{V_{cc}}{2R_{ph}}\right]K_i\cos(\theta-\delta_i) \\ &= I_{cc}K_i\cos(\theta-\delta_i) \\ &= \left[I_{cc}K_i\cos(\delta_i)\right]\cos(\theta)+\left[I_{cc}K_i\sin(\delta_i)\right]\sin(\theta) \\ &= I_q\cos(\theta)+I_d\sin(\theta) \end{aligned} \tag{11.87}$$

where the current amplitude I_p can be written as shown in terms of the zero speed or stall current $I_{cc} = V_{cc}/(2R_{ph})$ and a dimensionless scale factor K_i, where δ_i is the current phase angle, and where the last form describes the current in terms of the sum of a quadrature current component $I_q = I_{cc}K_i\cos(\delta_i)$ and a direct current component $I_d = I_{cc}K_i\sin(\delta_i)$.

The motor torque produced by the AC synchronous motor as derived in Chapter 9 and given by (9.17) applies in this situation. Substituting the amplitude of the back EMF from (11.86) and the current amplitude from (11.87) into (9.17) allows the motor torque to be written as a constant in the form

$$\begin{aligned} T &= \frac{3}{2} K_p I_p \cos(\delta_i) \\ &= \frac{3}{2}\left(\frac{V_{cc} N_m}{4\omega_{cc}}\right)\left(\frac{V_{cc}}{2R_{ph}} K_i\right)\cos(\delta_i) \\ &= \left(\frac{3V_{cc}^2 N_m}{16 R_{ph}\omega_{cc}}\right) K_i \cos(\delta_i) \\ &= \left(T_{cc}\right) K_i \cos(\delta_i) \end{aligned} \tag{11.88}$$

Once the motor and drive electronics are known, all parameters in (11.88) are constants except for the current amplitude scale factor K_i and current phase angle δ_i. For this reason, the last form in (11.88) identifies the collective constant terms as a torque constant T_{cc} since the remaining term $K_i\cos(\delta_i)$ describes the influence of phase current on torque production.

The two current parameters K_i and δ_i determine the torque capacity of the motor as limited and determined by the PWM duty cycle function parameters D and δ_d in (11.83) through the solution of (11.80). When $D = 1$, the motor drive electronics generate maximum possible applied voltage to the motor. When $\delta_i = 0$, the $\cos(\delta_i)$ term in (11.88) is equal to its maximum value of one.

Motor Current Solution

Without going through all the detailed mathematics, the solution of differential equation (11.80) using (11.82), (11.83), (11.85) and (11.87) gives the current amplitude scale factor as

$$K_i = D\left(\frac{\left(\cos(\delta_d) - \dfrac{\omega_e}{D\omega_{cc}}\right)^2 + \sin^2(\delta_d)}{1 + \left(Q_{cc}\dfrac{\omega_e}{\omega_{cc}}\right)^2}\right)^{1/2} \tag{11.89}$$

and the current phase angle as

$$\delta_i = \arctan\left(\frac{\sin(\delta_d)}{\cos(\delta_d) - \dfrac{\omega_e}{D\omega_{cc}}}\right) + \arctan\left(Q_{cc}\frac{\omega_e}{\omega_{cc}}\right) \tag{11.90}$$

where Q_{cc} is the dimensionless quantity